Dalton Transactions

ROYAL SOCIETY OF CHEMISTRY

PAPER

View Article Online
View Journal | View Issue

Cite this: *Dalton Trans.*, 2024, **53**, 16367

Luminescence of nanocrystalline BaFCl codoped with $Eu^{2+/3+}$ and Tb^{3+}†

Nishani T. Manamperi, Sachini W. Sivirathne, Alyssa M. Erlenbeck, S. Sameera Perera and Federico A. Rabuffetti *

Received 5th August 2024,
Accepted 17th September 2024

DOI: 10.1039/d4dt02237h

rsc.li/dalton

BaFCl:Eu,Tb nanocrystals were synthesized *via* hot-injection thermolysis of metal chlorodifluoroacetates and their luminescence response characterized between 80 and 430 K. Though unintended, partial reduction of Eu^{3+} to Eu^{2+} occurred during the synthesis stage, leading to luminescent nanocrystals coactivated by Eu^{2+}, Eu^{3+}, and Tb^{3+}. Their emission was dominated by Eu^{2+}, specifically by radiative transitions $4f^7$ ($^6P_{7/2}$) → $4f^7$ ($^8S_{7/2}$) and $4f^6 5d^1$ (lowest level) → $4f^7$ ($^8S_{7/2}$). Owing to the thermal coupling between $4f^7$ ($^6P_{7/2}$) and $4f^6 5d^1$ (lowest) levels, line-like emission from this manifold at 80 K evolved into band-like emission at 430 K. The change in the shape of the emission profile of Eu^{2+} was used to demonstrate that BaFCl:Eu,Tb may serve to realize bandshape luminescence thermometry as a more straightforward alternative to the usual ratiometric approach. The energy gap between $4f^7$ ($^6P_{7/2}$) and $4f^6 5d^1$ (lowest) levels and their radiative transition probabilities were estimated from time-resolved variable-temperature decays.

Introduction

Alkaline-earth fluorohalides of formula MFX (M = Ca, Sr, Ba; X = Cl, Br, I) have been extensively used as hosts for divalent (*e.g.*, Eu^{2+}) and trivalent rare-earth ions (*e.g.*, Sm^{3+}, Eu^{3+}, Er^{3+}, Tm^{3+}). Isovalent and aliovalent doping of these wide bandgap insulators render them functional materials on account of their photoluminescence and photochemical response. In this way, pressure[1–4] and temperature[5–7] luminescent sensors, photostimulable X-ray storage phosphors,[8–10] and photoexcitable storage phosphors sensitive to X-ray and UV-C radiation have been realized.[11–15] The crystal structure of fluorohalides and coordination polyhedra of rare-earth dopants (RE) are shown in Fig. 1. Fluorohalides display the archetypical matlockite structure. The unit cell is tetragonal and MF_4X_5 capped square antiprisms of C_{4v} symmetry serve as building blocks (Fig. 1a and b). The alkaline-earth metal has four fluoride and five heavy halide anions as nearest neighbors. The assembly of MF_4X_5 polyhedra leads to –F–M–X–X–M–F– double layers stacked along the *c* axis. Divalent rare-earth ions such as Eu^{2+} substitute for the alkaline-earth metal giving rise to $RE^{II}F_4X_5$ polyhedra (Fig. 1b).[16] In fact, EuFCl and EuFBr are well-known matlockite structures. By contrast, the local atomic environment of trivalent rare-earth dopants is still under debate. Knowledge of the symmetry of the site(s) occupied by these dopants ions was first gained *via* electron paramagnetic resonance[16–19] and later through fluorescence spectroscopy.[13,14,20,21] Recently, our group conducted X-ray absorption studies on Yb^{3+}-doped MFX nanocrystals and demonstrated that trivalent rare-earth ions do not sit in the matlockite structure as $RE^{III}F_4X_5$ polyhedra.[22] Instead, their first coordination shell consists of anionic donors of identical or similar radii. Two alternative models were proposed to

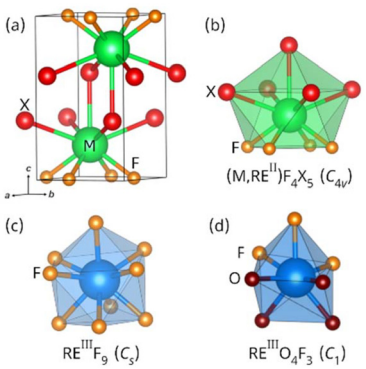

Fig. 1 (a) Unit cell of matlockite MFX. (b) Coordination polyhedra of divalent metals in the matlockite structure. (c and d) Possible coordination polyhedra of trivalent rare-earth metals.[22] Point group symmetries are indicated for each polyhedron.

Department of Chemistry, Wayne State University, Detroit, MI 48202, USA.
E-mail: far@chem.wayne.edu

†Electronic supplementary information (ESI) available: (1) thermal analysis of BaFCl:Eu,Tb nanocrystals, (2) refined structural parameters, (3) additional spectra and time-resolved decays, and (4) peak intensities used to compute $\tilde{\nu}_G^{Eu^{2+}}$. See DOI: https://doi.org/10.1039/d4dt02237h

rationalize experimental radial distribution functions. In the first model, the rare-earth coordination was described by a distorted capped square antiprism of formula $RE^{III}F_9$ and C_s symmetry (Fig. 1c). The second model entailed distorted capped trigonal prisms of formula $RE^{III}O_4F_3$ and C_1 symmetry (Fig. 1d). Insight into the local structure of rare-earth-doped fluorohalides is relevant to delineate energy-transfer pathways that directly impact photoluminescence response (*e.g.*, host-to-activator charge-transfer energies) and to establish the structural bases of photochemical reactions (*e.g.*, spatial correlation between electron and hole traps).

A distinct trait of alkaline-earth fluorohalides is their tunability. Chemical substitution of the metal (M) or of the heavy halogen (X) provides a lever to systematically tune structural and electronic features directly relevant to photoluminescence and photochemistry. On the structural side, chemical substitutions enable fine tuning of metal–halogen bond distances and covalency.[23] This tuning enables adjustment of, for example, the position of the $4f^{N-1}5d^1$ emissive levels of rare-earth dopants such as Sm^{2+} ($4f^6$) and Eu^{2+} ($4f^7$) relative to their ground states.[24–33] On the electronic side, chemical substitutions serve to tune band gaps,[34–36] which in turn impact the energy separation between rare-earth levels and band edges. The placement of the rare-earth activator ground and excited states relative to each other and to the host's band edges governs both photoluminescence (*e.g.*, charge-transfer excitation energies)[37,38] and photochemistry (*e.g.*, photo(thermal)ionization of RE^{2+} electron traps into the conduction band).[39] In parallel to achieving compositional control of structural and electronic features, using the phosphor's grain size to tailor functionality has gained traction over the past two decades. Transitioning from micron- to nano-sized crystals is obviously required in biophotonics.[40] When it comes to optical data storage, studies that unveiled the potential of rare-earth-doped alkaline-earth fluorides and fluorohalides as photoexcitable storage phosphors have indicated that size reduction positively impacts a number of aspects, including higher storage density (due to a higher concentration of oxygen defects), faster read out speed (due to shorter luminescence decays), and reduced energy consumption (due to lower bleaching thresholds).[11,13,41–43] As a result, advances have been made in the field of rare-earth-doped alkaline-earth fluorohalide nanophosphors. These advances encompass both synthetic developments and understanding of photoluminescence and photochemical response.

As a part of that effort, our group initiated an investigation of the luminescence of BaFCl:Eu^{3+},Tb^{3+} nanocrystals synthesized *via* hot-injection. At first, we aimed to exploit the well-known temperature-dependent Tb^{3+}-to-Eu^{3+} energy transfer[44–46] for luminescence thermometry purposes. Unexpectedly, we observed partial reduction of Eu^{3+} to Eu^{2+} during the synthesis stage, leading to BaFCl coactivated by Eu^{2+}, Eu^{3+}, and Tb^{3+}. More importantly, Eu^{2+} emission dominated the nanocrystals' response. To the best of our knowledge, reports on BaFCl codoped with mixed-valence europium are scarce.[47] In this article, we present a study of the luminescence of BaFCl:$Eu^{2+/3+}$,Tb^{3+} nanocrystals. Excitation, emission, and energy-transfer pathways are probed at room temperature and the temperature-dependent emission profile of Eu^{2+} is characterized between 80 and 430 K. The possibility of exploiting it for bandshape thermometry rather than ratiometric thermometry is discussed.

Experimental

Synthesis of BaFCl:Eu,Tb nanocrystals

Nanocrystal synthesis was carried out under nitrogen atmosphere using standard Schlenk techniques. $BaCO_3$ (99.98%), Eu_2O_3 (99.9%), $Tb(acac)_3$ (99.9%), $CF_2ClCOOH$ (98%), oleic acid (90%), 1-octadecene (90%), and trioctylphosphine (97%) were used as reagents. All chemicals were purchased from Sigma Aldrich and used without further purification. $CF_2ClCOOH$ and trioctylphosphine were stored under nitrogen. BaFCl:Eu,Tb nanocrystals (3.0 mol% of each codopant) were synthesized *via* hot-injection thermolysis of metal chlorodifluoroacetate precursors.[48] $BaCO_3$ (0.940 mmol), Eu_2O_3 (0.015 mmol), and $Tb(acac)_3$ (0.030 mmol) were added to a solution containing 3 mL of double-deionized water and 3 mL of $CF_2ClCOOH$. The resulting suspension was heated at 65 °C for 12 h until a colorless, optically transparent solution was obtained. Polycrystalline chlorodifluoroacetates were obtained after solvent evaporation at 65 °C for 48 h under a constant nitrogen flow rate of 200 mL min^{-1}. Once evaporation was completed, 4 mL of oleic acid and 1 mL of 1-octadecene were added to the flask containing metal precursors (flask A). 4 mL of oleic acid and 7 mL of 1-octadecene were added to a second flask (flask B). Flasks A and B were heated to 115 °C under vacuum (≈2 mTorr); magnetic stirring was employed throughout. After 45 min, flask B was switched to a nitrogen atmosphere, a thermocouple was placed inside the flask in direct contact with the solution, and 8 mL of trioctylphosphine were injected. Then, the temperature of flask B was increased to 275 °C and the solution in flask A was quickly injected. The reaction proceeded for 90 min at 275 °C and was quenched to room temperature using a stream of air. BaFCl:Eu,Tb nanocrystals were isolated by adding 40 mL of EtOH (200 proof) and centrifuging at 8000 rpm for 10 min. The resulting precipitate was resuspended using 5 mL of toluene, reprecipitated using 7 mL of EtOH and 2 mL of MeOH, centrifuged at 8000 rpm for 10 min, and dried in vacuum at room temperature. Polycrystalline BaFCl:Eu,Tb thus obtained was employed for chemical, morphological, structural, and luminescence analyses.

Powder X-ray diffraction (PXRD)

PXRD patterns were collected using a Bruker D2 Phaser diffractometer operated at 30 kV and 10 mA. Cu Kα radiation (λ = 1.5418 Å) was employed. A nickel filter was used to remove Cu Kβ. Diffractograms were collected in the 10–70° 2θ range using a step size of 0.012° and a step time of 1.5 s.

Transmission electron microscopy (TEM)

TEM images were obtained using a Thermo Scientific Talos F200X G2 S/TEM microscope operated at 200 kV. Nanocrystals were dispersed in methanol and sonicated for 30 min. Then, a drop of the resulting suspension was deposited on a 200 mesh Cu grid coated with a Lacey carbon film (Ted Pella Inc.).

Rietveld analysis

Rietveld analysis[49,50] of PXRD data was performed using the General Structure Analysis System II (GSAS-II).[51] The average crystal structure of BaFCl:Eu,Tb nanocrystals was refined using the tetragonal *P*4/*nmm* space group. The following parameters were refined: (1) scale factor; (2) background, which was modeled using a shifted Chebyschev function; (3) instrument parameters, including diffractometer constant and contributions to peak profile; (4) lattice constants (*a* and *c*); (5) fractional atomic coordinates of barium (*z*Ba) and chlorine (*z*Cl); (6) an isotropic displacement parameter for each of the atoms in the structure (U_{Ba}, U_F, and U_{Cl}, constrained to $U_F = 3U_{Ba}$ and $U_{Cl} = 2U_{Ba}$); and (7) crystallite size and microstrain. Difference curve and R_w residual were employed to assess the quality of the refinement. Crystal structure and metal coordination polyhedra were visualized using VESTA.[52]

X-ray photoelectron spectroscopy (XPS)

Nanocrystals were analyzed using a Thermo Scientific Nexsa X-ray photoelectron spectrometer equipped with a hemispherical analyzer and monochromatic Al Kα sources (1486.7 eV). ≈10 mg of the sample were mounted on a regular sample holder using conductive copper tapes; care was taken to ensure a flat surface. The holder was then loaded into the entry-lock chamber and held under vacuum for more than 30 min. Once the vacuum level reached 4×10^{-7} mbar, the sample was transferred from the entry-lock to the analysis chamber, which was kept at a base pressure of $\approx 1.8 \times 10^{-7}$ mbar throughout data acquisition. High-resolution spectra were collected for C 1s, Eu 3d, and Ba 3p core lines using a pass energy of 50 eV, an energy step size of 0.1 eV, and 100 ms per step as the dwell time. Qualitative and quantitative spectral analyses were performed using Thermo Avantage. The C 1s core line at 284.8 eV was employed for charge referencing. All peaks were fitted using pseudo-Voigt functions.

Spectrofluorometry

Luminescence analyses were conducted using a Fluorolog 3–222 fluorometer (Horiba Scientific). A xenon lamp and a 265 nm SpectraLED (Horiba Scientific) were used as excitation sources for steady-state and time-resolved measurements, respectively. A photomultiplier tube R928 (Hammamatsu Photonics) served as the detector. Steady-state spectra and time-resolved decays were first collected under ambient conditions and then variable-temperature measurements were conducted. For the latter, BaFCl:Eu,Tb nanocrystals were loaded into a VPF–800 variable-temperature stage (Lake Shore Cryotronics) and degassed at 450 K for 2 h under vacuum (≈50 mTorr) prior to data collection. Heating to 450 K (177 °C) had no effect on the chemical and structural integrity of the nanocrystals as shown by X-ray diffraction and thermal analysis (see ESI, Fig. S1†). Temperature control was provided by a Lake Shore 335–3060 controller. Spectra and decays were collected in the 80–430 K temperature window using slit widths ranging between 1 and 2 nm. A heating rate of 10 K min^{-1} was employed throughout. Nanocrystals were allowed to dwell for ≈20 min at the target temperature prior to data collection. All spectrofluorometric analyses were conducted using BaFCl:Eu,Tb polycrystalline solids that had not been exposed to X-ray radiation.

Results and discussion

A PXRD pattern and a representative TEM image of BaFCl:Eu,Tb nanocrystals are given in Fig. 2. Rietveld analysis confirmed the phase purity of polycrystalline BaFCl:Eu,Tb as all diffraction maxima in the pattern were indexed to the fluorochloride phase (PDF No. 024–0096); no secondary crystalline phases were observed (Fig. 2a). Refined unit cell constants, atomic coordinates, and isotropic displacement parameters are given in the ESI (see Table S1†). Diffraction maxima exhibited anisotropic microstrain broadening which complicated adequate modeling of some reflection profiles, notably that of (101) ($2\theta \approx 23.7°$). From a morphological standpoint, nanocrystals showed irregular spherical shape with an average diameter of 26.5 nm (Fig. 2b). These results were in line with those previously reported by our group for BaFCl:Yb,Er nanocrystals synthesized *via* hot-injection thermolysis of metal chlorodifluoroacetates.[48] For completeness, we note that rare-earth solubility curves for BaFCl nanocrystals synthesized using the procedure described herein had shown rare-earth doping efficiencies of 90% up to a total concentration of 6 mol%.[48]

We then proceeded to screen the room-temperature luminescence response of the nanocrystals. Results from these

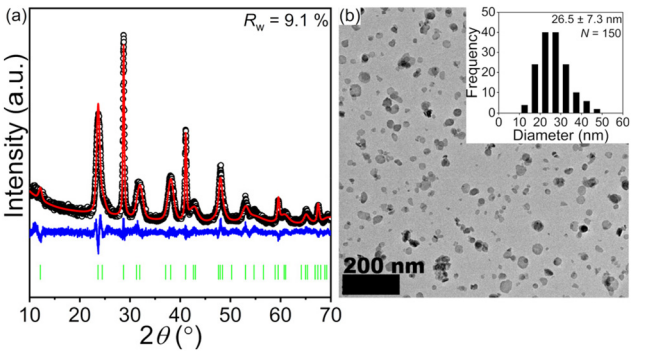

Fig. 2 (a) Rietveld analysis of the PXRD pattern of BaFCl:Eu,Tb nanocrystals. Experimental data (black circles), calculated pattern (red line), difference curve (blue line, offset for clarity), and tick marks corresponding to the calculated diffraction maxima are shown (green vertical bars). (b) Electron microscopy image and nanocrystal size distribution histogram (inset).

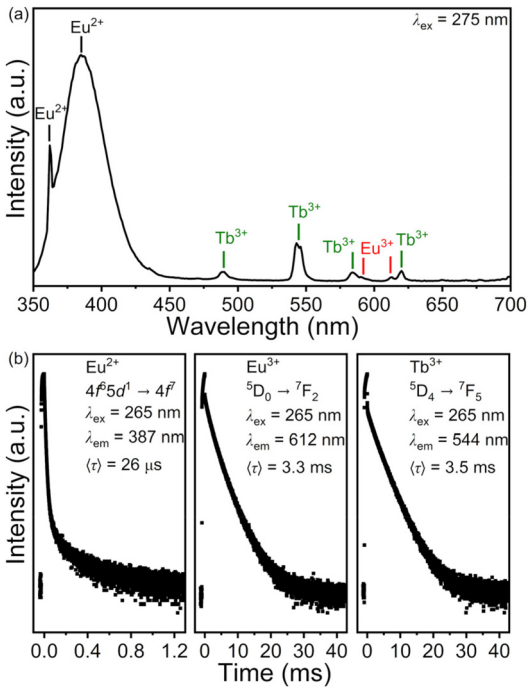

Fig. 3 Room-temperature emission spectrum (a) and time-resolved luminescence decays (b) of BaFCl:Eu,Tb nanocrystals. Decays are plotted in logarithmic scale.

studies are summarized in Fig. 3. An emission spectrum collected under 275 nm excitation revealed the presence of three emitting centers: Eu^{2+}, Eu^{3+}, and Tb^{3+} (Fig. 3a). The spectrum was dominated by a broad band peaking at 387 nm arising from radiative relaxation of the lowest level of the Eu^{2+} $4f^65d^1$ excited state (hereafter referred to as $4f^65d^1$ (ll)) to the $4f^7$ ($^8S_{7/2}$) ground state. In addition, line emission resulting from the $4f^7$ ($^6P_{7/2}$) → $4f^7$ ($^8S_{7/2}$) zero-phonon transition of Eu^{2+} was observed at 363 nm. Emissions from 4f–4f transitions of Eu^{3+} and Tb^{3+} were much weaker and appeared at 486 (Tb^{3+}, $^5D_4$ → $^7F_6$), 544 (Tb^{3+}, $^5D_4$ → $^7F_5$), 584 (Tb^{3+}, $^5D_4$ → $^7F_4$), 592 (Eu^{3+}, $^5D_0$ → $^7F_1$), 612 (Eu^{3+}, $^5D_0$ → $^7F_2$), and 620 nm (Tb^{3+}, $^5D_4$ → $^7F_3$). Excited-state lifetimes extracted from time-resolved luminescence decays were consistent with the presence of Eu^{2+}, Eu^{3+}, and Tb^{3+} activators (Fig. 3b). Intensity-weighted average lifetimes ($\langle\tau\rangle$) equal to 26 μs (Eu^{2+}, $4f^65d^1$ (ll) → $4f^7$), 3.3 ms (Eu^{3+}, $^5D_0$ → $^7F_2$), and 3.5 ms (Tb^{3+}, $^5D_4$ → $^7F_5$) were estimated using eqn (1), where $I(t)$ is the baseline-corrected

$$\langle\tau\rangle = \frac{\int I(t)t\mathrm{d}t}{\int I(t)\mathrm{d}t} \quad (1)$$

intensity at time t. Similar average lifetimes were extracted *via* multiexponential fits (see ESI, Fig. S2†). The average lifetime obtained for Eu^{2+} in our BaFCl:Eu,Tb nanocrystals is in line with values previously reported for Eu^{2+}-doped BaFCl.[24,53] All decays were nonexponential, pointing to multisite distribution of each activator within the nanocrystals and/or energy transfer between activators. While emissions from Eu^{3+} and Tb^{3+} were obviously expected, the presence of Eu^{2+} was rather surprising considering that $Eu^{III}_2O_3$ was used as the europium precursor and that no reducing agent was deliberately introduced at any point during nanocrystal synthesis. Incorporation of Eu^{2+} into micro- and nanocrystalline BaFX has been extensively reported but solids were invariably synthesized under a reducing atmosphere (*e.g.*, N_2/H_2)[24,27,54] or using a divalent europium precursor (*e.g.*, EuF_2).[55–57] Alternatively, Eu^{2+} may be generated *via* X-ray induced photoreduction of Eu^{3+} doped into BaFCl and BaFBr; however, this was not the case here. As mentioned earlier, luminescence analyses were conducted using BaFCl:Eu,Tb nanocrystals that had not been exposed to X-ray radiation. Thus, partial reduction of Eu^{3+} to Eu^{2+} occurred during the synthesis stage. At the present time, we are unable to pinpoint the reducing species responsible for this transformation. Control experiments showed that partial reduction of Eu^{3+} also took place during the preparation of singly-doped BaFCl:Eu nanocrystals and of nanocrystals codoped with different Eu : Tb ratios (see ESI, Fig. S3†).

We attempted to estimate the Eu^{3+} : Eu^{2+} ratio in BaFCl:Eu,Tb nanocrystals using X-ray photoelectron spectroscopy. However, a europium concentration of 3 mol% was too low to obtain a reliable estimate of that ratio. Thus, we performed XPS analyses on BaFCl:Eu nanocrystals featuring a 4 mol% europium concentration. Results from these analyses are shown in Fig. 4. The high-resolution Eu 3d spectrum exhibited peaks in the $3d_{5/2}$ and $3d_{3/2}$ regions and a complex shape due to the presence of shake-up and shake-down features. Nonetheless, well-established peak-fit guidelines[58–60] enabled peak deconvolution and extraction of qualitative and quantitative information. The spectrum was dominated by an intense peak at ≈1136.6 eV. This peak was deconvoluted into Ba $3p_{1/2}$ and Eu $3d_{5/2}$ contributions while maintaining the area ratio of 1 : 2 between the Ba $3p_{3/2}$ and Ba $3p_{1/2}$ spin–orbit components. Deconvolution resulted in two peaks centered at ≈1135.6 and ≈1137.0 eV assigned to Eu $3d_{5/2}$ (Eu^{3+}) and Ba $3p_{3/2}$ core lines, respectively. Though the Eu $3d_{5/2}$ peak arising from Eu^{3+}

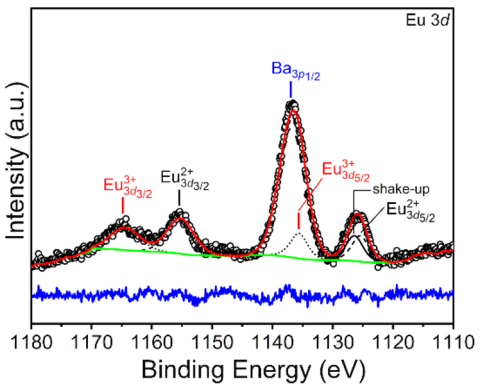

Fig. 4 High-resolution Eu 3d XPS spectrum of BaFCl:Eu (4 mol%) nanocrystals. Experimental data (black circles), calculated spectrum (red line), background (green line), and difference curve (blue line, offset for clarity) are shown. Also shown are deconvoluted peaks corresponding to Eu^{2+} (short-dashed black line), Eu^{3+} (dotted black line), Ba 3p core (dashed black line), and shake-up features (solid black line).

showed a strong overlap with the Ba $3p_{1/2}$ peak, the Eu $3d_{3/2}$ peak centered at ≈1164.7 eV unequivocally confirmed the presence of Eu^{3+}. The presence of Eu^{2+} was confirmed by Eu $3d_{5/2}$ and Eu $3d_{3/2}$ peaks centered at ≈1125.9 and ≈1155.6 eV, respectively. The areas of the Eu $3d_{5/2}$ peaks corresponding to Eu^{3+} and Eu^{2+} were computed and translated to atomic percentages, which were subsequently used to estimate the Eu^{3+} : Eu^{2+} ratio. A value of 0.8 was thus obtained, indicating that ≈56% of the Eu^{3+} in the initial reaction mixture had been reduced to Eu^{2+} (n.b., assuming that the calculated ratio was representative of the entire nanocrystal volume). Su and Sun observed $Eu^{3+} \rightarrow Eu^{2+}$ reduction in bulk solids synthesized under nitrogen or air atmosphere, but the extent of the reaction was significantly lower (<2%).[47]

Room-temperature excitation spectra of BaFCl:Eu,Tb, BaFCl:Tb, and BaFCl:Eu nanocrystals were collected to gain insight into energy-transfer pathways between activators. Results from these studies are presented in Fig. 5. The excitation spectrum of the Eu^{2+} 387 nm emission in BaFCl:Eu,Tb was dominated by a broad band with maxima at 260 and 272 nm (Fig. 5a), which we assign to excitation from the $4f^7$ ($^8S_{7/2}$) ground state of Eu^{2+} to the upper levels of the $4f^65d^1$ excited state.[61–63] A very similar excitation profile was observed for the 544 nm emission of Tb^{3+}, although in this case maxima were located at 265 and 275 nm. Additionally, a weak peak arising from the 4f–4f excitation of Tb^{3+} was observable at 377 nm ($^7F_6 \rightarrow {}^5L_{10}$). The similarity between the excitation spectra of Eu^{2+} and Tb^{3+} and the observation of emission from the latter upon excitation of the former pointed to the occurrence of $Eu^{2+} \rightarrow Tb^{3+}$ energy transfer. Comparison of the excitation spectra of BaFCl:Eu,Tb and BaFCl:Tb nanocrystals gave further support to this conclusion. The spectrum of BaFCl:Tb featured a broad band around 250 nm, which we assign to the $4f^8 \rightarrow 4f^75d^1$ transition of Tb^{3+}, as well as a number of weak peaks arising from 4f–4f transitions (Fig. 5b). Codoping BaFCl:Tb with europium led to the appearance of the band peaking at 275 nm, *i.e.*, of a new excitation pathway in which the $4f^65d^1$ excited state of Eu^{2+} fed Tb^{3+} emission. In the case of the 612 nm emission of Eu^{3+} in BaFCl:Eu,Tb, the excitation spectrum displayed a broad band around 250 nm (Fig. 5a). Moreover, a peak corresponding to the 4f–4f excitation of Eu^{3+} appeared at 393 nm ($^7F_0 \rightarrow {}^5L_6$). The excitation profile is similar to that observed in singly-doped BaFCl:Eu nanocrystals (Fig. 5c). Based on previous studies of Eu^{3+}-doped BaFCl,[20,47,64] we assign the band around 250 nm to a charge-transfer state involving the top of the valence band (vb) and the ground state of Eu^{3+} (*i.e.*, $e_{vb} + Eu^{3+}(^7F_6) \rightarrow h_{vb}^{+} + Eu^{2+}(^8S_{7/2})$). The position of the $^8S_{7/2}$ ground state of the transient Eu^{2+} generated during this electron transfer ought to be distinguished from that of the Eu^{2+} centers generated in the synthesis stage because they sit in different crystallochemical environments, as mentioned in the Introduction. Excitation of BaFCl:Eu nanocrystals using 240 nm light (≈5.2 eV) led to excitation of both Eu^{3+} (*via* charge transfer, ≈5.0 eV) and Eu^{2+} (*via* $4f^7$ ($^8S_{7/2}$) $\rightarrow 4f^65d^1$, ≈4.5 eV) and subsequent emissions at 612 and 387 nm (Fig. 5d). Decreasing the excitation energy favored

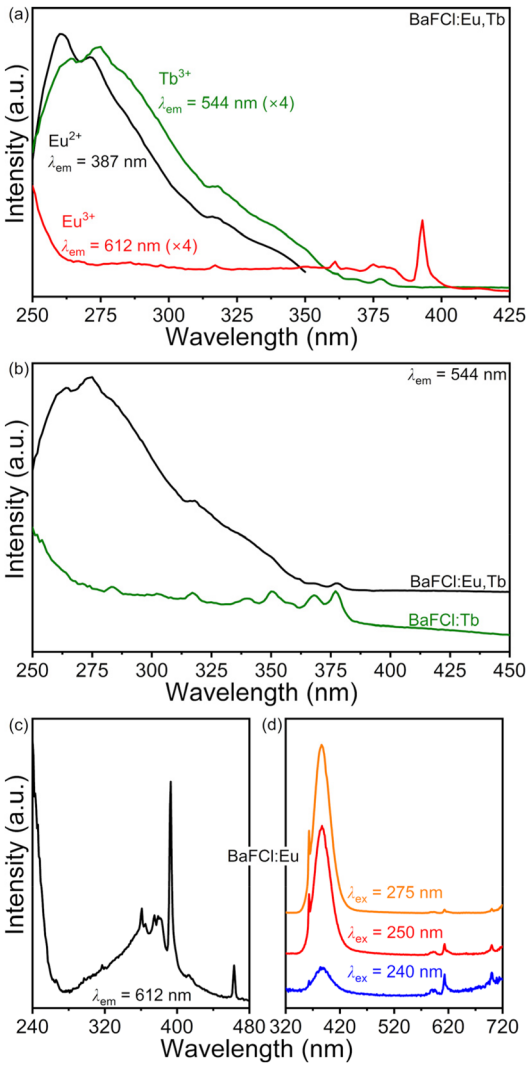

Fig. 5 (a) Excitation spectra of BaFCl:Eu,Tb nanocrystals. (b) Excitation spectrum of BaFCl:Tb (6 mol%) nanocrystals. The spectrum of BaFCl:Eu,Tb is also shown to facilitate comparison. (c) and (d) show the excitation and emission spectra of BaFCl:Eu (6 mol%) nanocrystals. Spectra were collected at room temperature.

excitation of Eu^{2+} in detriment of Eu^{3+} as shown by a decrease in the intensity of Eu^{3+} emission relative to that of Eu^{2+}. Similar to what was observed for BaFCl:Eu, excitation of BaFCl:Eu,Tb nanocrystals using 275 nm light led to very weak Eu^{3+} emission (Fig. 5a). In summary, excitation of BaFCl:Eu,Tb at 275 nm populated the upper levels of the $4f^65d^1$ excited state of Eu^{2+}. Subsequently, this led to Eu^{2+} emissions at 363 and 387 nm *via* radiative relaxation of the $4f^7$ ($^6P_{7/2}$) and $4f^65d^1$ (*ll*) levels, respectively. The $4f^65d^1$ excited state of Eu^{2+} also served to feed Tb^{3+} $4f^8$ ($^5D_4$) $\rightarrow 4f^8$ (^7F_J) emissions *via* $Eu^{2+} \rightarrow Tb^{3+}$ energy transfer. Excitation at 275 nm also induced Eu^{3+} $4f^6$ ($^5D_0$) $\rightarrow 4f^6$ (^7F_J) emissions *via* a host $\rightarrow Eu^{3+}$ charge-transfer state. For completeness we note that excitation of the terbium-centered $^7F_6 \rightarrow {}^5D_4$ transition at 486 nm led to Eu^{3+} emission, indicating the occurrence of $Tb^{3+} \rightarrow Eu^{3+}$ energy transfer (see

ESI, Fig. S4†). Tb^{3+} emission bands were not observed upon excitation of the $^7F_0 \rightarrow {}^5D_2$ transition of Eu^{3+} at 463 nm, suggesting that $Eu^{3+} \rightarrow Tb^{3+}$ energy transfer did not take place.

Emission spectra excited at 275 nm were collected between 80 and 430 K to assess the potential of BaFCl:Eu,Tb nanocrystals as luminescence thermometers. Results from these studies are compiled in Fig. 6. Spectra featured the expected emissions from Eu^{2+}, Eu^{3+}, and Tb^{3+} (Fig. 6a). At first, the temperature dependence of four major bands was of interest to us; these were $4f^7$ ($^6P_{7/2}$) → $4f^7$ ($^8S_{7/2}$) of Eu^{2+} at 27 550 cm^{-1}, $4f^65d^1$ (*ll*) → $4f^7$ ($^8S_{7/2}$) of Eu^{2+} at ≈25 800 cm^{-1}, $^5D_4 \rightarrow {}^7F_5$ of Tb^{3+} at 18 334 cm^{-1}, and the red emission band including the $^5D_0 \rightarrow {}^7F_2$ of Eu^{3+} at 16 334 cm^{-1} and the $^5D_4 \rightarrow {}^7F_3$ of Tb^{3+} at 16 139 cm^{-1}. However, visual inspection of the spectra led us to focus on the emissions from Eu^{2+}. Indeed, the most noticeable change was the decrease in the intensity of the f–f line emission at 27 550 cm^{-1} and the simultaneous increase of the fd–f broad band emission at ≈25 800 cm^{-1} upon increasing temperature. This change was simply the result of the thermal coupling between the $4f^7$ ($^6P_{7/2}$) and $4f^65d^1$ (*ll*) levels of Eu^{2+}, with the former sitting a few hundred wavenumbers below the latter (*vide infra*). Thermal coupling between these two levels is well-documented for Eu^{2+} doped into a number of hosts, including BaFCl.[24,25,27,53,56,63] The temperature dependence of the integrated intensities of the four bands of interest further confirmed the potential of the $4f^65d^1$ (*ll*)/$4f^7$ ($^6P_{7/2}$) manifold for temperature sensing. The emission intensity from the lower thermally coupled level dropped by ≈2 orders of magnitude upon going from 80 to 430 K whereas that of the upper level showed a threefold increase up to 230 K and plateaued afterwards (Fig. 6b). Relative intensity changes between the green (Tb^{3+}) and red band (Eu^{3+} and Tb^{3+}) were significantly less pronounced. Nonetheless, using the $4f^65d^1$ (*ll*)/$4f^7$ ($^6P_{7/2}$) manifold for ratiometric thermometry is not straightforward due to the strong overlap between their emission bands, which complicates extraction of *accurate* integrated intensities and of the corresponding luminescence intensity ratios.[27,65] Eu^{2+} intensities plotted in Fig. 6b were extracted by fitting spectra between 20 000 and 30 000 cm^{-1} with a varying number of gaussians (13 at 80 K, 7 at 430 K). We thought of two alternatives to the luminescence intensity ratio. First, we considered computing the geometric centroid of the Eu^{2+} emission. However, this involves integration limits that change with temperature, thus compromising accuracy and repeatability. Next, we attempted using a peak-intensity-weighted centroid ($\tilde{\nu}_G^{Eu^{2+}}(T)$) as the thermometric parameter. We defined this centroid using eqn (2). Here, $I_{f\rightarrow f}^{\tilde{\nu}_1}$ and $I_{fd\rightarrow f}^{\tilde{\nu}_2}$ are the peak intensities of the emissions from the $4f^7$ ($^6P_{7/2}$) and $4f^65d^1$ (*ll*) levels measured at wavenumbers $\tilde{\nu}_1$ and $\tilde{\nu}_2$, respectively. The use of $\tilde{\nu}_G^{Eu^{2+}}(T)$ as the thermometric parameter does not require setting arbitrary integration limits nor performing peak fit. Further, it can be computed on the fly once wavenumbers $\tilde{\nu}_1$ and $\tilde{\nu}_2$ are set. In this work, we set $\tilde{\nu}_1 = 27\,548\ cm^{-1}$ (363 nm) and $\tilde{\nu}_2 = 25\,774\ cm^{-1}$ (388 nm) and computed $\tilde{\nu}_G^{Eu^{2+}}$ using the corresponding peak intensities at each temperature (see ESI, Table S2†). $\tilde{\nu}_G^{Eu^{2+}}$ decreased from 27 316 to 26 338 cm^{-1} upon going from 80 to 430 K (Fig. 6c). The sigmoidal dependence of $\tilde{\nu}_G^{Eu^{2+}}(T)$ was adequately modeled using a Boltzmann

$$\tilde{\nu}_G^{Eu^{2+}}(T) = \frac{I_{f\rightarrow f}^{\tilde{\nu}_1}(T) \times \tilde{\nu}_1 + I_{fd\rightarrow f}^{\tilde{\nu}_2}(T) \times \tilde{\nu}_2}{I_{f\rightarrow f}^{\tilde{\nu}_1}(T) + I_{fd\rightarrow f}^{\tilde{\nu}_2}(T)} \quad (2)$$

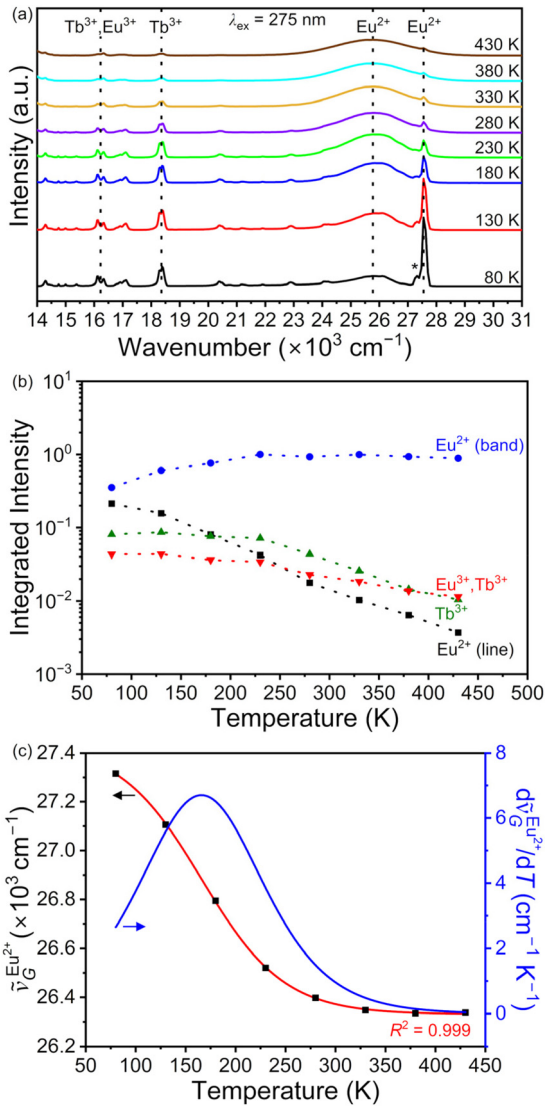

Fig. 6 (a) Variable-temperature emission spectra of BaFCl:Eu,Tb nanocrystals. Four emissions of interest are depicted with dotted lines. The temperature dependence of their integrated intensities is given in (b). Intensities are normalized with respect to the broad band of Eu^{2+} at 230 K. The integrated intensity of Eu^{2+} line emission corresponds to that of the zero-phonon line at 27 550 cm^{-1}; the one-phonon line at 27 315 cm^{-1} (depicted with an asterisk) was not included in the integration. (c) Experimental (black squares, eqn (2)) and calculated (red line, eqn (3)) temperature dependence of the peak-intensity-weighted centroid of Eu^{2+} emission. The derivative of the calculated dependence is also plotted (blue line).

function given by eqn (3). This phenomenological model reflected the transition from line emission at low temperature

$$\tilde{\nu}_{G}^{Eu^{2+}}(T) = A_2 + \frac{A_1 - A_2}{1 + \exp\frac{T - T_0}{\sigma}} \quad (3)$$

($4f^7$ ($^6P_{7/2}$) → $4f^7$ ($^8S_{7/2}$)) to broad band emission at high temperatures ($4f^65d^1$ (*ll*) → $4f^7$ ($^8S_{7/2}$)). The corresponding fit parameters were A_1 = 27 437(13) cm^{-1}, A_2 = 26 331(11) cm^{-1}, T_0 = 166(2) K, and σ = 41(1) K. The temperature sensitivity of the centroid was maximum at 165 K, with a shift of 6.7 cm^{-1} K^{-1} (Fig. 6c). Altogether, results from these studies demonstrated that the temperature-dependent change in the emission profile of Eu^{2+} may be exploited to realize bandshape luminescence thermometry as a straightforward alternative to the traditional ratiometric approach.

Finally, we aimed to gain quantitative insight into the thermosensitive $4f^65d^1$ (*ll*)/$4f^7$ ($^6P_{7/2}$) manifold of Eu^{2+} doped into BaFCl:Eu,Tb nanocrystals. Specifically, we sought to estimate the energy gap between these two thermally coupled levels (ΔE), their radiative transition probabilities ($k_{fd\rightarrow f}$, $k_{f\rightarrow f}$), and compare these values to those reported for micron-sized Eu^{2+}-doped BaFCl.[24,27,53] Previous studies used eqn (4) to

$$R(T) = \frac{g_f}{g_d} \times \frac{k_{f\rightarrow f}}{k_{fd\rightarrow f}} \times \exp\frac{\Delta E}{kT} \quad (4)$$

fit the temperature dependence of the luminescence intensity ratio to estimate the energy gap. Here, g_f and g_d are the degeneracies of the emissive levels (g_f/g_d = 4).[27] These fits, however, ran into problems due to the challenge of extracting accurate integrated intensities from emission spectra. Sytsma and Blasse explicitly acknowledged this issue.[27] Liu and coworkers estimated the energy gap using just three experimental $R(T)$ values between 10 and 216 K. Some $R(T)$ values computed using eqn (4) deviated more than 20% from their experimental counterparts.[53] Sommerdijk and coworkers used just two experimental data points, R(77 K) and R(300 K).[24] Further, authors did not provide enough details to assess the quality of the fits (*e.g.*, fit plot and residual and/or a complete set of fit parameters). On this basis, we decided to estimate photophysical parameters of the $4f^65d^1$ (*ll*)/$4f^7$ ($^6P_{7/2}$) manifold using the temperature dependence of its radiative constant ($k_{Eu^{2+}}$) as given by eqn (5). Here $\langle\tau\rangle$ is the

$$k_{Eu^{2+}}(T) = \frac{1}{\tau} = \frac{k_{f\rightarrow f} + k_{fd\rightarrow f} \times (g_d/g_f) \times \exp[-\Delta E/(kT)]}{1 + (g_d/g_f) \times \exp[-\Delta E/(kT)]} \quad (5)$$

intensity-weighted average lifetime of Eu^{2+} emission computed using eqn (1) (*vide supra*). Luminescence decays were excited at 265 nm and emission was monitored at 387 nm between 80 and 325 K, a temperature range comparable to that employed in previous studies of Eu^{2+}-doped BaFCl.[24,27,53] The resulting temperature-dependence of $k_{Eu^{2+}}$ is plotted in Fig. 7; experimental decays are given in the ESI (see Fig. S5†). Eqn (5) provided a good fit to experimental $k_{Eu^{2+}}$ values. The corresponding fit parameters were ΔE = 205(27) cm^{-1}, $k_{f\rightarrow f}$ = 5212(2643) s^{-1}, and $k_{fd\rightarrow f}$ = 5.1 × 10^5 (4.4 × 10^4) s^{-1}. Though

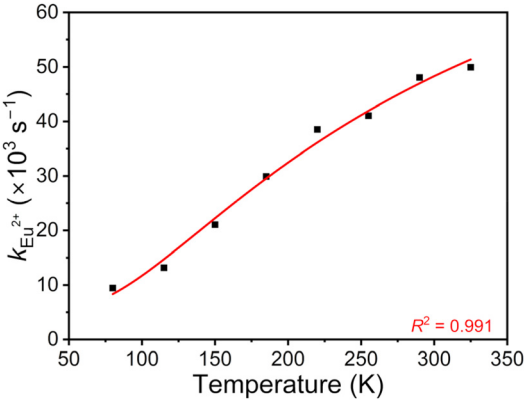

Fig. 7 Experimental (black squares) and calculated (red line, eqn (5)) temperature-dependence of the radiative constant of Eu^{2+} in BaFCl:Eu,Tb nanocrystals.

slightly smaller, the $4f^65d^1$ (*ll*)/$4f^7$ ($^6P_{7/2}$) energy gap estimated for our nanocrystals is in the same range of that previously reported for BaFCl:Eu^{2+} single crystals and bulk solids (393, 400, and 592 cm^{-1}).[24,27,53] A similar remark holds for radiative transition probability $k_{f\rightarrow f}$ (5212 s^{-1} *vs.* 4000 s^{-1}).[24,27,53] In the case of $k_{fd\rightarrow f}$, our value was smaller than those reported in the literature (5.1 × 10^5 s^{-1} *vs.* 1.5 × 10^6, 3.5 × 10^6, and 1.6 × 10^7 s^{-1}).[24,27,53] $k_{fd\rightarrow f}$ and $k_{f\rightarrow f}$ differed by two orders of magnitude, as expected for the probabilities of parity-allowed *vs.* parity-(and spin)-forbidden transitions, respectively.

Conclusions

The luminescence response of BaFCl:$Eu^{2+/3+}$,Tb^{3+} nanocrystals was characterized between 80 and 430 K. Although trivalent europium was used as a reagent and no reducing agent was deliberately incorporated in the reaction mixture, partial reduction to divalent europium occurred during the synthesis stage. The resulting Eu^{3+}/Eu^{2+} ratio was estimated to be *ca.* 0.8, corresponding to a reduction of over half of the starting Eu^{3+} ions. The room-temperature emission spectrum of BaFCl:$Eu^{2+/3+}$,Tb^{3+} was dominated by near UV emissions from the $4f^7$ ($^6P_{7/2}$) and $4f^65d^1$ (*ll*) thermally coupled levels of Eu^{2+}. Emission from this manifold transitioned from line-like to band-like upon increasing temperature, a feature that could be exploited for bandshape luminescence thermometry. We introduced the peak-intensity-weighted centroid as an alternative thermometric parameter that circumvents a number of issues arising in the context of ratiometric thermometry. Photophysical parameters of the $4f^65d^1$ (*ll*)/$4f^7$ ($^6P_{7/2}$) manifold were estimated from time-resolved variable-temperature decays and should help to establish composition–luminescence relationships in nanocrystalline alkaline-earth fluorohalides as the nanocrystal library expands.

Data availability

All the data used are provided in the article and the ESI.†

Conflicts of interest

There are no conflicts to declare.

Acknowledgements

The authors would like to acknowledge the financial support of the National Science Foundation (DMR-2003118) and of Wayne State University (Department of Chemistry and Office of the Vice President for Research). They also thank the Lumigen Instrument Center at Wayne State University for the use of the X-ray diffraction (National Science Foundation MRI-1427926), electron microscopy (National Science Foundation MRI-2018587), and photoelectron spectroscopy facilities (National Science Foundation MRI-1849578).

References

1 Y. R. Shen, T. Gregorian and W. B. Holzapfel, Progress in Pressure Measurements with Luminescence Sensors, *High Pressure Res.*, 1991, **7**, 73–75.
2 P. Comodi and P. F. Zanazzi, Improved Calibration Curve for the Sm^{2+}-BaFCl Pressure Sensor, *J. Appl. Crystallogr.*, 1993, **26**, 843–845.
3 Y. R. Shen, U. Englisch, L. Chudinovskikh, F. Porsch, R. Haberkorn, H. P. Beck and W. B. Holzapfel, A Structural Study on the PbFCl-Type Compounds MFCl (M = Ba, Sr, and Ca) and BaFBr Under High-Pressure, *J. Phys.: Condens. Matter*, 1994, **6**, 3197–3206.
4 B. Lorenz, Y. R. Shen and W. B. Holzapfel, Characterization of the New Luminescence Pressure Sensor SrFCl:Sm^{2+}, *High Pressure Res.*, 1994, **12**, 91–99.
5 S. S. Perera, K. T. Dissanayake and F. A. Rabuffetti, Alkaline-Earth Fluorohalide Nanocrystals for Upconversion Thermometry, *J. Lumin.*, 2019, **207**, 416–423.
6 B. D. Dhanapala, H. N. Munasinghe, K. T. Dissanayake, L. Suescun and F. A. Rabuffetti, Expanding the Synthetic Toolbox to Access Pristine and Rare-Earth-Doped BaFBr Nanocrystals, *Dalton Trans.*, 2021, **50**, 16092–16098.
7 B. D. Dhanapala, H. N. Munasinghe and F. A. Rabuffetti, Temperature-Dependent Luminescence of CaFCl:Yb,Er Upconverting Nanocrystals, *J. Lumin.*, 2021, **235**, 117974.
8 M. Sonoda, M. Takano, J. Miyahara and H. Kato, Computed Radiography Utilizing Scanning Laser Stimulated Luminescence, *Radiology*, 1983, **148**, 833–838.
9 K. Takahashi, J. Miyahara and Y. Shibahara, Photostimulated Luminescence (PSL) and Color-Centers in BaFCl-Eu^{2+}, BaFBr-Eu^{2+}, BaFI-Eu^{2+} Phosphors, *J. Electrochem. Soc.*, 1985, **132**, 1492–1494.
10 K. Takahashi, K. Kohda, J. Miyahara, Y. Kanemitsu, K. Amitani and S. Shionoya, Mechanism of Photostimulated Luminescence in BaFX:Eu^{2+} (X = Cl, Br) Phosphors, *J. Lumin.*, 1984, **31–32**, 266–268.
11 H. Riesen and W. A. Kaczmarek, Efficient X-ray Generation of Sm^{2+} in Nanocrystalline BaFCl/Sm^{3+}: A Photoluminescent X-ray Storage Phosphor, *Inorg. Chem.*, 2007, **46**, 7235–7237.
12 N. Riesen, A. François, K. Badek, T. M. Monro and H. Riesen, Photoreduction of Sm^{3+} in Nanocrystalline BaFCl, *J. Phys. Chem. A*, 2015, **119**, 6252–6256.
13 H. Riesen, K. Badek, T. M. Monro and N. Riesen, Highly Efficient Valence State Switching of Samarium in BaFCl:Sm Nanocrystals in the Deep UV for Multilevel Optical Data Storage, *Opt. Mater. Express*, 2016, **6**, 3097–3108.
14 J. Zhang and H. Riesen, Controlled Generation of Tm^{2+} Ions in Nanocrystalline BaFCl:Tm^{3+} by X-ray Irradiation, *J. Phys. Chem. A*, 2017, **121**, 803–809.
15 N. Riesen, C. Priest, D. G. Lancaster, K. Badek and H. Riesen, Ultra-High-Resolution Greyscale Fluorescence Images via UV-Exposure of Thin Flexible Phosphor Films, *Nanoscale*, 2023, **15**, 4863–4869.
16 D. Nicollin and H. Bill, Gd^{3+}, Eu^{2+} in SrFCl and BaFCl Single Crystals: EPR Results, *Solid State Commun.*, 1976, **20**, 135–137.
17 D. Zevenhuijzen, J. A. Vanwinsum and H. W. D. Hartog, S-State, Ions in Tetragonal SrFCl, *J. Phys. C: Solid State Phys.*, 1976, **9**, 3113–3119.
18 D. Nicollin and H. Bill, Experimental Contribution to the Study of the S-State Ions in Ionic Single-Crystals, *J. Phys. C: Solid State Phys.*, 1978, **11**, 4803–4814.
19 M. Falin, H. Bill and D. Lovy, EPR of Sm^{3+} in BaFCl Single Crystals, *J. Phys.: Condens. Matter*, 2004, **16**, 1293–1298.
20 Q. Ju, Y. S. Liu, R. F. Li, L. Q. Liu, W. Q. Luo and X. Y. Chen, Optical Spectroscopy of Eu^{3+}-Doped BaFCl Nanocrystals, *J. Phys. Chem. C*, 2009, **113**, 2309–2315.
21 Z. Liu, M. A. Stevens-Kalceff and H. Riesen, Effects of Postannealing on the Photoluminescence Properties of Coprecipitated Nanocrystalline BaFCl:Sm^{3+}, *J. Phys. Chem. A*, 2013, **117**, 1930–1934.
22 D. K. Amarasinghe, K. T. Dissanayake, B. D. Dhanapala and F. A. Rabuffetti, Local Atomic Environment of Yb^{3+} in Alkaline-Earth Fluorohalide Nanocrystals, *CrystEngComm*, 2022, **24**, 5317–5323.
23 K. T. Dissanayake and F. A. Rabuffetti, Multicolor Emission in Chemically and Structurally Tunable Er:Yb:SrFX (X = Cl, Br) Upconverting Nanocrystals, *Chem. Mater.*, 2018, **30**, 2453–2462.
24 J. L. Sommerdijk, J. M. P. J. Verstegen and A. Bril, Luminescence of MeFX:Eu^{2+} (Me = Sr, Ba; X = Cl, Br), *J. Lumin.*, 1974, **8**, 502–506.
25 T. Kobayasi, S. Mroczkowski, J. F. Owen and L. H. Brixner, Fluorescence Lifetime and Quantum Efficiency for $5d \rightarrow 4f$ Transitions in Eu^{2+} Doped Chloride and Fluoride Crystals, *J. Lumin.*, 1980, **21**, 247–257.
26 R. Jaaniso and H. Bill, f–f and f–d Transition Interference in Sm^{2+}:SrFCl, *Phys. Rev. B: Condens. Matter Mater. Phys.*, 1991, **44**, 2389–2392.

27 J. Sytsma and G. Blasse, Comparison of the Emission of Eu^{2+} in MFCl (M = Sr, Ba) and Gd^{3+} in YOCl, *J. Lumin.*, 1992, **51**, 283–292.
28 Y. R. Shen and W. B. Holzapfel, Effect of Pressure on Energy Levels of Sm^{2+} in BaFCl and SrFCl, *Phys. Rev. B: Condens. Matter Mater. Phys.*, 1995, **51**, 15752–15762.
29 Y. Shen and K. L. Bray, Effect of Pressure and Temperature on 4f–4f, Luminescence Properties of Sm^{2+} ions in *M*FCl crystals (*M* = Ba, Sr, and Ca), *Phys. Rev. B: Condens. Matter Mater. Phys.*, 1998, **58**, 11944–11958.
30 P. Pal, T. Penhouet, V. D'Anna and H. Hagemann, Effect of Temperature and Pressure on Emission Lifetime of Sm^{2+} Ion Doped in MFX (M = Sr, Ba; X = Br, I) Crystals, *J. Lumin.*, 2013, **142**, 66–74.
31 P. Pal, H. Hagemann, H. Bill and J. Zhang, Temperature and Host Dependence of the Transition Interference between f–f and f–d Transitions of Sm^{2+} in Matlockites, *J. Lumin.*, 2015, **161**, 323–329.
32 J. Afshani, T. Delgado, G. Paveliuc, P. Pal and H. Hagemann, Optical Properties of Sm^{2+} Doped in BaFI Crystals, *J. Lumin.*, 2023, **257**, 119648.
33 C. van Aarle, K. W. Krämer and P. Dorenbos, Lengthening of the Sm^{2+} $4f^5 5d \rightarrow 4f^6$ Decay Time Through Interplay With the $4f^6[^5D_0]$ Level and its Analogy to Eu^{2+} and Pr^{3+}, *J. Lumin.*, 2024, **266**, 120329.
34 E. Nicklaus, Optical Properties of Some Alkaline Earth Halides, *Phys. Status Solidi A*, 1979, **53**, 217–224.
35 V. V. Mikhailin and M. A. Terekhin, Luminescence Excitation of Barium Fluorohalides by Using Synchrotron Radiation, *Nucl. Instrum. Methods Phys. Res., Sect. A*, 1989, **282**, 607–609.
36 G. Kalpana, B. Palanivel, I. B. Shameem Banu and M. Rajagopalan, Structural and Electronic Properties of Alkaline-earth Fluorohalides Under Pressure, *Phys. Rev. B: Condens. Matter Mater. Phys.*, 1997, **56**, 3532–3535.
37 P. Dorenbos, Systematic Behaviour in Trivalent Lanthanide Charge Transfer Energies, *J. Phys.: Condens. Matter*, 2003, **15**, 8417–8434.
38 P. Dorenbos, Thermal Quenching of Lanthanide Luminescence via Charge Transfer States in Inorganic Materials, *J. Mater. Chem. C*, 2023, **11**, 8129–8145.
39 J. J. Schuyt and G. V. M. Williams, Quenching of the Sm^{2+} Luminescence in $NaMgF_3$:Sm via Photothermal Ionization: Alternative Method to Determine Divalent Lanthanide Trap Depths, *Appl. Phys. Lett.*, 2019, **115**, 181104.
40 X. Zhao, Q. Yu, J. Yuan, N. V. Thakor and M. C. Tan, Biodegradable Rare Earth Fluorochloride Nanocrystals for Phototheranostics, *RSC Adv.*, 2020, **10**, 15387–15393.
41 M. A. Stevens-Kalceff, Z. Liu and H. Riesen, Cathodoluminescence Microanalysis of Irradiated Microcrystalline and Nanocrystalline Samarium Doped BaFCl, *Microsc. Microanal.*, 2012, **18**, 1229–1238.
42 N. Chowdhury, N. Riesen and H. Riesen, Efficient Generation of Stable Sm^{2+} in Nanocrystalline $BaLiF_3$:Sm^{3+} by UV- and X-Irradiation, *J. Phys. Chem. C*, 2019, **123**, 25477–25481.
43 E. Aboelezz and B. W. Pogue, Review of Nanomaterial Advances for Ionizing Radiation Dosimetry, *Appl. Phys. Rev.*, 2023, **10**, 021312.
44 M. T. Berry, P. S. May and Q. Hu, Calculated and Observed Tb^{3+} $(^5D_4) \rightarrow Eu^{3+}$ Electronic Energy Transfer Rates in $Na_3[Tb_{0.01}Eu_{0.99}(oxydiacetate)_3]\cdot 2NaClO_4\cdot 6H_2O$, *J. Lumin.*, 1997, **71**, 269–283.
45 M. Bettinelli, A. Speghini, F. Piccinelli, J. Ueda and S. Tanabe, Energy Transfer Processes in $Sr_3Tb_{0.90}Eu_{0.10}(PO_4)_3$, *Opt. Mater.*, 2010, **33**, 119–122.
46 G. Bao, K.-L. Wong, D. Jin and P. A. Tanner, A Stoichiometric Terbium–Europium Dyad Molecular Thermometer: Energy Transfer Properties, *Light: Sci. Appl.*, 2018, **7**, 96.
47 M.-Z. Su and X.-P. Sun, Luminescence and Possible Electron Transfer and Transitions in BaFCl:Eu Crystal, *Mater. Res. Bull.*, 1987, **22**, 879–886.
48 K. T. Dissanayake, D. K. Amarasinghe, L. Suescun and F. A. Rabuffetti, Accessing Mixed-Halide Upconverters Using Heterohaloacetate Precursors, *Chem. Mater.*, 2019, **31**, 6262–6267.
49 H. M. Rietveld, Line Profiles of Neutron Powder-Diffraction Peaks for Structure Refinement, *Acta Crystallogr.*, 1967, **22**, 151–152.
50 H. M. Rietveld, A Profile Refinement Method for Nuclear and Magnetic Structures, *J. Appl. Crystallogr.*, 1969, **2**, 65–71.
51 B. H. Toby and R. B. Von Dreele, GSAS-II: The Genesis of a Modern Open-Source All-Purpose Crystallography Software Package, *J. Appl. Crystallogr.*, 2013, **46**, 544–549.
52 K. Momma and F. Izumi, VESTA 3 for Three-dimensional Visualization of Crystal, Volumetric and Morphology Data, *J. Appl. Crystallogr.*, 2011, **44**, 1272–1276.
53 G. K. Liu, X. Y. Chen and J. Huang, Intensity and Bandwidth of Multiphonon Vibronic Transitions of Rare-earth Ions in Crystals, *Mol. Phys.*, 2003, **101**, 1029–1036.
54 X. Zhang, Y. Wang, J. Liu, G. Zhang, G. Xiong and X. Xu, Temperature Dependence of the Photostimulated Luminescence of BaFCl:Eu^{2+} After Ultraviolet Irradiation, *J. Appl. Phys.*, 1995, **78**, 1984–1986.
55 W. Chen, S. Wang, S. L. Westcott, J. Zhang, K. Dou, A. G. Joly and D. E. McCready, Structure and Luminescence of BaFBr:Eu^{2+} and BaFBr:Eu^{2+},Tb^{3+} Phosphors and Thin Films, *J. Appl. Phys.*, 2005, **97**, 083506.
56 M. Secu, C. Secu, V. Vasile, D. Predoi and D. Gazdaru, Time-Resolved Luminescence Spectroscopy of Eu^{2+} in BaFCl:Eu^{2+} X-ray Storage Phosphor, *J. Optoelectron. Adv. Mater.*, 2007, **9**, 1800–1802.
57 G. Gundiah, E. Bourret-Courchesne, G. Bizarri, S. M. Hanrahan, A. Chaudhry, A. Canning and W. W. Moses, S. E. Derenzo, in Scintillation Properties of Eu^{2+}-Activated Barium Fluoroiodide, IEEE Nuclear Science Symposium Conference, 2009, pp. 1575–1578.
58 W.-D. Schneider, C. Laubschat, I. Nowik and G. Kaindl, Shake-up Excitations and Core–Hole Screening in Eu

Systems, *Phys. Rev. B: Condens. Matter Mater. Phys.*, 1981, **24**, 5422–5425.

59 R. Vercaemst, D. Poelman, R. L. Van Meirhaeghe, L. Fiermans, W. H. Laflère and F. Cardon, An XPS Study of the Dopants' Valence States and the Composition of $CaS_{1-x}Se_x$:Eu and $SrS_{1-x}Se_x$:Ce Thin Film Electroluminescent Devices, *J. Lumin.*, 1995, **63**, 19–30.

60 F. Mercier, C. Alliot, L. Bion, N. Thromat and P. Toulhoat, XPS Study of Eu(III) Coordination Compounds: Core Levels Binding Energies in Solid Mixed Oxocompounds $Eu_mX_xO_y$, *J. Electron Spectrosc. Relat. Phenom.*, 2006, **150**, 21–26.

61 T. J. A. Popma, W. F. van der Weg and K. Thimm, Excitation of Luminescent Materials by Synchrotron Radiation, *J. Lumin.*, 1981, **24–25**, 289–292.

62 A. M. Gurvich and V. V. Mikhailin, Crystal Phosphors for Storage Luminescent Screens, *Russ. Chem. Rev.*, 1992, **61**, 576.

63 W. Chen, N. Kristianpoller, A. Shmilevich, D. Weiss, R. Chen and M. Su, X-ray Storage Luminescence of BaFCl:Eu^{2+} Single Crystals, *J. Phys. Chem. B*, 2005, **109**, 11505–11511.

64 M.-Z. Su and X.-P. Sun, The Charge Transfer Excitation of Trivalent Rare Earth Ions Sm^{3+}, Eu^{3+}, Gd^{3+}, Ho^{3+}, Er^{3+} and Yb^{3+} Emission in BaFCl Crystals, *Mater. Res. Bull.*, 1987, **22**, 89–94.

65 M. Sójka, M. Runowski, T. Zheng, A. Shyichuk, D. Kulesza, E. Zych and S. Lis, Eu^{2+} Emission from Thermally Coupled Levels–New Frontiers for Ultrasensitive Luminescence Thermometry, *J. Mater. Chem. C*, 2022, **10**, 1220–1227.